Optics Design and Optimizations of the Multi-color TES Bolometer Camera for the ASTE Telescope

Tatsuya Takekoshi, Tetsuhiro Minamidani, Shunichi Nakatsubo, Tai Oshima, Masayuki Kawamura,
Hiroshi Matsuo, Tatsuhiro Sato, Nils W. Halverson, Adrian T. Lee, William L. Holzapfel, Yoichi Tamura,
Akihiko Hirota, Kenta Suzuki, Takuma Izumi, Kazuo Sorai, Kotaro Kohno and Ryohei Kawabe

Abstract—**Wideband continuum observations at the millimeter and submillimeter wavelengths are of great importance to the understanding of the cosmic history of star-formation across the Hubble time, as well as the thermal and non-thermal aspects of clusters of galaxies through the Sunyaev-Zel'dovich effect. To promote such studies, a new TES bolometer camera for the ASTE telescope has been developed. In this article we present the study of the optics system that will couple the camera to the telescope's Cassegrain optics. Two-color simultaneous observation capability and 7.5 arcminute diameter FoV are achieved. These two focal planes are used for the 270 and 350 GHz Bands for Phase I, and the 350 and 670 GHz Bands for Phase II configurations. The numbers of pixels are 169, 271, and 919 pixels for 270, 350, and 670 GHz Bands, respectively. The shape of the third ellipsoid mirror is optimized, and the designed optics is foreseen to be diffraction limited. The optics is also evaluated via physical optics calculations, and the diameter of the cold pupil is optimized to 85% of the geometrical design. Without filters and Ruze losses, the aperture efficiencies of each beam are ∼35%, 35%, and 32%, and the beam sizes are ∼28, 22, and 12 arcseconds, for the 270, 350, and 670 GHz Bands, respectively.**

Index Terms—**Submillimeter wave, astronomy, optics**

I. INTRODUCTION

IT is of great importance to astronomy and astrophysics to understand the star-formation history of galaxies from distant to nearby (from early to recent universe), and the evolution of cosmic large scale structure. The redshift distribution of (sub)millimeter-bright galaxies (SMGs) is a clue to understanding the cosmic star-formation history. Understanding of the physics of the interstellar media in the Milky Way and nearby galaxies is also important in revealing the masses or density structures of molecular gas in which stars are formed. Spatial and kinematic structures of galaxy clusters obtained via high-resolution mapping of the Sunyaev-Zel'dovich (SZ) effect enable us to probe the dynamic evolutional history of clusters.

There is a sizable number of studies (e.g., Coppin et al. 2006 [1]) of SMGs, clusters of galaxies, nearby galaxies, and Milky Way sources using SCUBA on JCMT [2], MAMBO on IRAM 30-m telescope [3], Bolocam on CSO [4], and AzTEC on JCMT [5]. The AzTEC instrument mounted on the ASTE telescope has enabled wide and deep observations of over 1 $\deg^2$ area down to 0.5–1 mJy/beam depth, and more than 1000 SMGs have been detected at the 1.1 mm wavelength [6]–[14]. Recent developments of the large formatted submillimeter bolometer arrays, such as SCUBA2 on JCMT [15] and LABOCA on APEX telescope [16], will open a window to large and deep surveys at submillimeter wavelength. The Spitzer Space Telescope [17] and the Herschel Space Observatory [18] are surveying large areas from near- to far-infrared wavelengths ($\leq 500\mu$m). While the Atacama Large Millimeter/submillimeter Array (ALMA) provides the highest angular resolution and sensitivity, its field of view (FoV) is quite limited. Under such circumstances, multiband photometry by array receivers at millimeter to submillimeter wavelengths is critical to defining the spectrum energy distributions (SEDs) of these objects. Thus, we aim to develop a new millimeter and submillimeter bolometer camera for the ASTE telescope.

The Atacama Submillimeter Telescope Experiment (ASTE) [19], [20] is a 10-m submillimeter telescope located at an altitude of 4860m at Pampa la Bola in the Atacama Desert in northern Chile. The Atacama Desert is one of the best sites for millimeter and submillimeter wave astronomy due to its high atmospheric transmission [21]. Among the viable atmospheric windows at the Atacama Desert, we carefully chose the 270, 350, and 670 GHz atmospheric windows. These three frequency windows are suitable for detection and redshift determination of SMGs from SEDs. Furthermore, the multi-color optics system that is capable of simultaneous observations of two or three frequency bands will improve the observing efficiency and calibration capability. Therefore, it is necessary to design and develop a re-imaging optics to couple the focal plane bolometers to the Cassegrain optics of the ASTE telescope.

In this paper, we report the details of the optics design of the multi-color continuum camera for the ASTE telescope.

TABLE I
OBSERVING BANDS OF NEW BOLOMETER CAMERA FOR ASTE

Bands	Frequency range (GHz)	Band width (GHz)
270 GHz Band	244–294	50
350 GHz Band	330.5–365.5	35
670 GHz Band	630–710	80

TABLE II
HORN DIMENSIONS

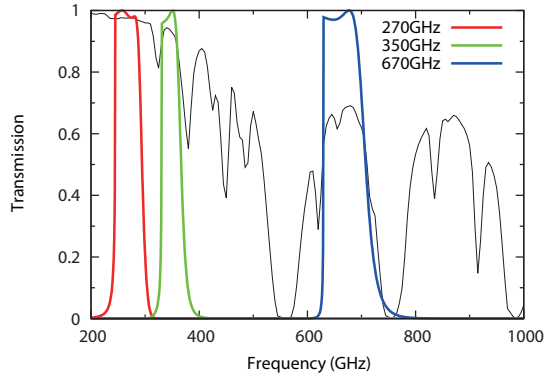| Phase Band	I 270 GHz	I/II 350 GHz	II 670 GHz
Aperture diameter (mm)	3.65	3.65	1.815
Total flare angle (degree)	12.7	12.7	12.7
Flare length (mm)	16.50	16.50	8.205

Fig. 1. Normalized observing bands of the new continuum camera for the ASTE telescope. The solid curve is the atmospheric transmission the Atacama Desert [21] under best conditions (0.284 mm pwv).

In Section II, considerations and detailed optics design are described. In Section III, evaluations using physical optics are described and we discuss the results. We give a brief summary in Section IV.

II. OPTICS DESIGN

In this section, we describe the requirements for the optics design, the preliminary design, the detail design, and the comparison of simulated performance with the requirements.

A. Requirements and Constraints for Optics Design

1) Scientific Requirements: A large FoV is necessary for both fast mapping speed and the retrieval of weak and extended astronomical signals. For ground telescopes, signals from astronomical objects are buried under strong atmospheric emission. The atmospheric emission is usually removed utilizing the fact that it is seen over the whole array while the astronomical object is confined to some extent. Therefore, a considerable fraction of extended astronomical emissions whose sizes are comparable to or larger than the FoV are also removed [22].

The bandwidths are determined to be as wide as possible while avoiding the water vapor absorptions to achieve good sensitivities. The frequency bands are summarized in Table I, and the passbands are shown in Figure 1 with the atmospheric transmission curve at the ASTE site.

2) Limitations from detectors: The focal plane detectors, Transition Edge Sensor (TES) bolometer arrays, were designed based on the South Pole Telescope 150 GHz arrays [23] and modifications to match higher frequencies were introduced [24]. The major diameter of a hexagonal wafer is set to 85

mm to fit in a 4-inch fabrication process, which imposes the maximum focal plane size to be 70 mm in diameter when considering the wiring space. A maximum of 448 and 1152 readout channels are available for Phase I and II, respectively. We adopt the identical array design for the 270 and 350 GHz wafers to save design cost and time, hence the same pixel separation. In this case, the numbers of pixels of hexagonal arrays are 271, 271, and 919 pixels for the 270, 350, and 670 GHz Bands, respectively. We can use only the central 169 pixels for the 270 GHz Band because of the limitation of the readout number in the Phase I operations. The diameter of the central 169 pixels of the 270 GHz Band wafer corresponds to 55 mm.

TES bolometer arrays are coupled to free-space via conical horn arrays. This requires a flat focal plane and image-side telecentric optics. The aperture diameter of the horn is set by the separations of bolometers. The flare angle of 12.7 degrees is chosen to use the same tooling as for the APEX-SZ instrument [25]. The parameters of the conical horns are shown in Table II.

3) Limitations from the Receiver Cabin of the ASTE Telescope and the Cryogenics: First, all the optics components and the cryostat should fit in a receiver cabin which is approximately 1.9 m in length × 2.2 m in width × 1.8 m in height, with one of its corner spaces occupied by a 19-inch standard rack (Figure 5). Second, it is a Cassegrain cabin, which tilts in accordance with the elevation angle of the telescope (Figure 2). In addition, the cooling power of pulse-tube cooler used as a pre-cooler to 4K varies with orientation and constrains the tilt angle to 30 degrees. Therefore, the optical axis of the cryostat is tilted 30 degrees from that of the telescope to maximize the observable elevation angle range, from 30 to 90 degrees, while keeping the pulse-tube cooler within 30 degrees of vertical.

B. Preliminary Design

Under these requirements and limitations we design an optics that couples to the Cassegrain system of the ASTE telescope whose antenna parameters are summarized in Table III. The ASTE telescope has a classical Cassegrain optics whose F-number is 8.878. Figure 3 shows the relationship of the Cassegrain system and the receiver cabin. The Cassegrain focus is located above the ceiling of the receiver cabin, and rays reflected by the main- and sub-reflectors go into the receiver cabin while outspreading. Thus, it is necessary to have a re-imaging mirror in the receiver cabin.

The re-imaging mirror is designed as an ellipsoidal mirror to refocus the outspreading rays into a focal plane in the
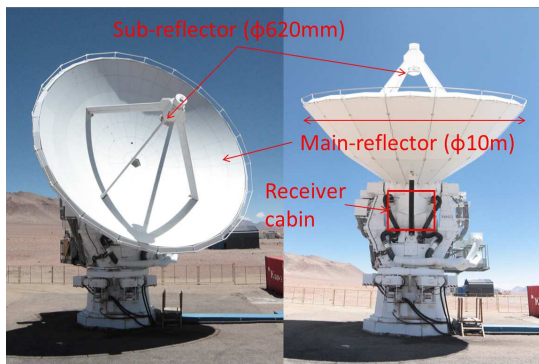
Fig. 2. The ASTE telescope. The Cassegrain system consists of a 10-m main-reflector and a 620-mm sub-reflector. The receiver cabin and the Cassegrain system move together with the elevation angle.

TABLE III
ANTENNA PARAMETERS OF ASTE TELESCOPE

Main-reflector dia.	10 m
Sub-reflector dia.	620 mm
F/#	8.878
Surface accuracy	19 μm r.m.s.
Mainbeam efficiency	0.6-0.7 (350 GHz)
Beam size	22" (350 GHz)
Pointing accuracy	2" r.m.s.

cryostat. Figure 4 shows the optics in the receiver cabin. Due to the limited space available in the receiver cabin and to minimize the number of optical elements, this ellipsoidal mirror is located very close to the floor of the receiver cabin, and requires an aperture diameter of 560 mm (Figure 5). The achieved 7.5 arcminutes FoV is the maximum possible size under the limitations of the available receiver cabin space.

The cryostat window is placed at a certain position to avoid the interference with rays between the sub-reflector and the re-imaging ellipsoidal mirror. This position limits the size of the cold optics to about a 500 mm cube.

Figures 6 and 7 show the cold optics inside the cryostat and its schematic diagram. Incident rays are divided into two bands by a metal mesh dichroic filter [26] that is placed at the pupil to reduce the filter aperture size. This is a key component to realize simultaneous multi-color optics without reducing the observing efficiency. However, the small inclination angle of the dichroic filter to the incident principle ray is required to keep good transmission and reflection characteristics, thus we limit it to 25 degrees. This is a strong constraint to realize simultaneous three band optics in the physical space available for our cryostat. Therefore, we concentrate on the design for the simultaneous two bands observations. Hereafter, we will refer to the reflected band as "Band 1" and the transmitted band as "Band 2". The orthographic views of Bands 1 and 2 are shown in Figures 8 and 9. We assign these bands to the 270 and 350 GHz Bands, respectively, for Phase I configuration, and to the 670 and 350 GHz Bands, respectively, for Phase II configuration (see also Table VI). We use low pass and high pass dichroic filters for Phase I and Phase II, respectively.
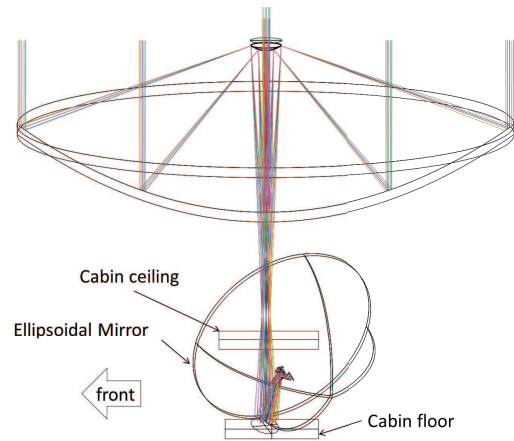

Fig. 3. Physical relationship of the Cassegrain system to the receiver cabin.
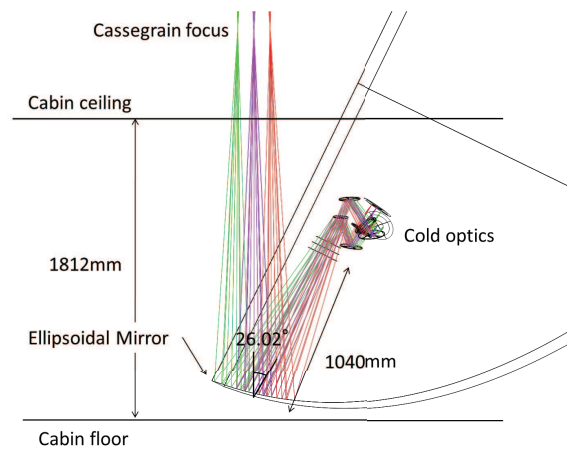

Fig. 4. Side view of the receiver cabin and optics cut along the incident-reflected plane of the ellipsoidal mirror. The ray from the Cassegrain system focuses near the ceiling of the receiver cabin.

The holder of the dichroic filters is blackend with the Stycast 2850FT filled with SiC grains of size ~ 1000 μm [27], which works as the cold pupil to reduce the optical load on the bolometers. The optimization of its size is described in Section III-C1, and has 85% of the diameter of the geometrical pupil.

The rays split by the dichroic filter are reflected by plane mirrors respectively to make a compact cold optics. In each band, a dielectric lens is placed between the dichroic filter and a horn array to make a telecentric system and to fit the size of the focal plane. For Band 1, an additional flat mirror is used between the dielectric lens and the horn array.

C. Detail Designs and Optimization

1) Iterative Optimization of the Re-Imaging Ellipsoidal Mirror (The Third Mirror "M3"): The preliminary ellipsoidal mirror causes large aberrations especially at the edges of the field of view, and modification is necessary to realize the diffraction-limited performance over the FoV and all frequency bands. We optimize the shape of the third mirror as a modified
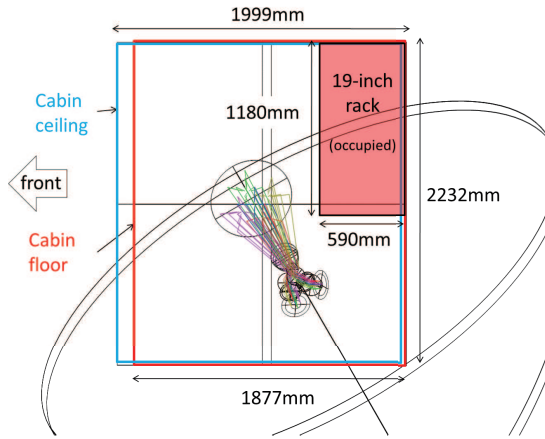
Fig. 5. Top view of the receiver cabin and optics. The space occupied by the 19-inch standard rack limits the maximum size of the third re-imaging mirror.

Fig. 8. The orthographic views of Band 1 (670 GHz) cold optics. The 270 and 670 GHz Bands are operated in Phases I and II respectively.
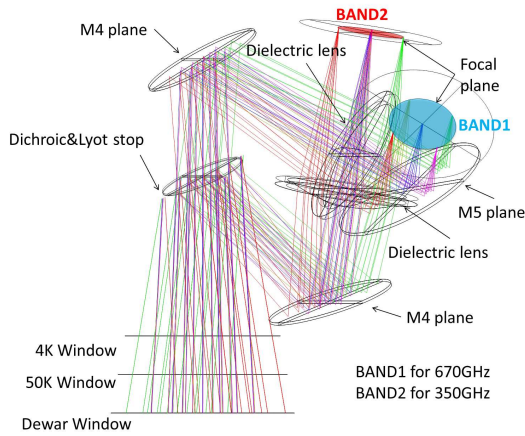

Fig. 6. Side view of Phase II cold optics cut along the incident-reflected plane of the ellipsoidal mirror. The ray reflected by the ellipsoidal mirror goes through the 300 K, 50 K, and 4 K windows. The dichroic filter divides incoming rays into two bands, and each ray is focused after flat mirrors and HDPE lenses.
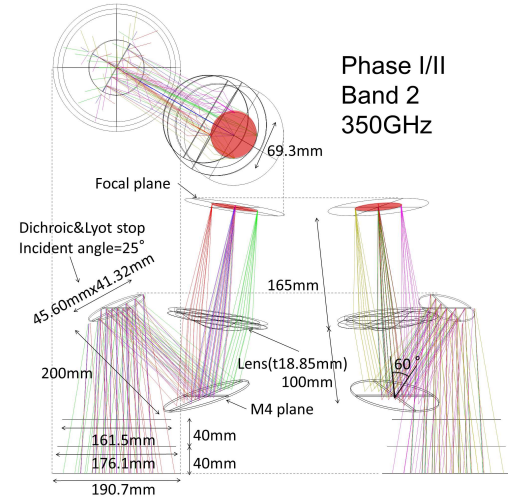
Fig. 9. The orthographic views of Band 2 cold optics. 350 GHz Band is operated in Phase I and II.

ellipsoid that is expressed as:

$$z(r) = \frac{cr^2}{1 + \sqrt{1 - (1+k)c^2r^2}} + a_1r + a_2r^2 + a_3r^3 + a_4r^4 + a_5r^5$$

where r is distance from the major axis z of ellipsoid, c is the curvature ($c = 1/R$ where R is the curvature radius), k is the conic constant, and $a_i(i = 1 - 5)$ represents the polynomial modification coefficients. These modification parameters are optimized using ZEMAX [28], a ray tracing software. In ZEMAX, the merit function, which correlates to the lateral aberration, is used as an index for this optimization and is minimized. The merit function has five parameters that correspond to the coefficients of fifth order polynomials.

After the optimization of the third mirror, it is necessary to check not only the imaging quality over the FoV and all frequency bands but also the space limitations in the receiver cabin and cryostat. We manually adjust the design over many
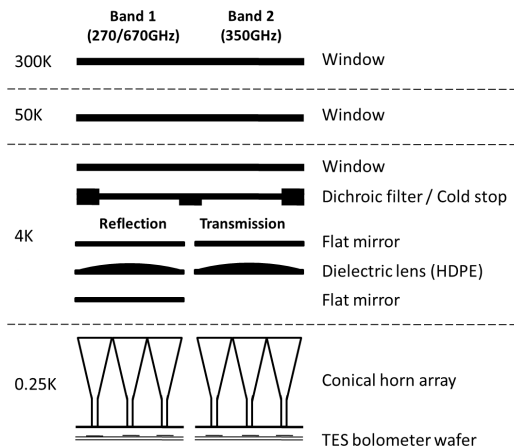

Fig. 7. Schematic diagram showing optical components in the cryostat. The beams divided by dichroic filter into higher and lower frequency bands are focused with dielectric lenses, and coupled with conical horns.
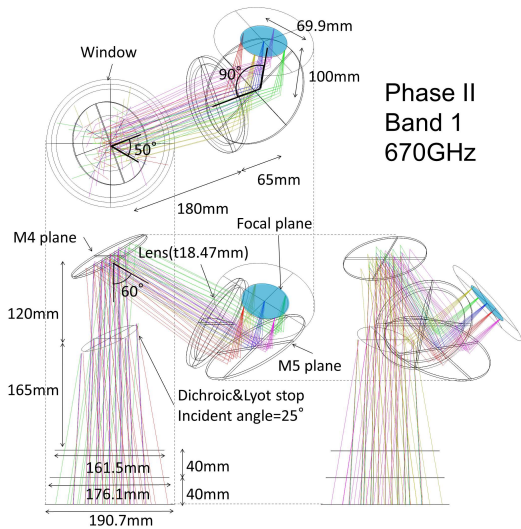
optimization cycles by hand to satisfy these conditions. Finally, this results the optimized modified ellipsoidal mirror with the following parameters:

$$R = 1879.702\text{mm},$$
$$k = -0.118,$$
$$a_1 = 0.317,$$
$$a_2 = -2.157 \times 10^{-5},$$
$$a_3 = -3.890 \times 10^{-8},$$
$$a_4 = -1.684 \times 10^{-12},$$
$$a_5 = 1.973 \times 10^{-15}.$$

Parameters before the above optimization are $R = 1879.702$mm, $k = -0.118$, and all polynomial modification coefficients, $a_i = 0$ ($i = 1 - 5$). This corresponds to an ellipsoid whose length from the telescope's Cassegrain focus to the third mirror is 2213.714 mm and from the third mirror to another focus is 2050 mm with a reflection angle of 20 degrees. The optimization terms change the incident angle to the third mirror to 13.01 degrees.

2) Dielectric Lens: High density polyethylene (HDPE) was chosen as a material for the dielectric lenses because of its low absorption coefficient at millimeter to submillimeter wavelengths [29]. Since the physical properties such as thermal contraction and refractive index of polymers can vary by manufacturing process, lenses were designed based on the measurement of these properties.

To estimate the thermal contraction rate of our HDPE sample from 300 K to 4K, the sample was immersed in liquid nitrogen and the thermal contraction rate to 77 K was measured to be 1.91 ± 0.02 as a lower limit. To obtain the upper limit, we extrapolate this value to 4K by using the thermal contraction rate of Teflon [30], which is larger than that of HDPE. Hence we conclude the thermal contraction rate from 300 K to 4 K of HDPE to be 2.0 ± 0.1 percent, which is consistent with previous studies [31].

The refractive indices of the HDPE at ~ 20 K were measured using the Fourier transform spectrometer (FTS) and Indium Antimonide (InSb) bolometer. To avoid inhomogeneity in our 200 mm diameter HDPE sample due to porosity, the porous inner 100 mm diameter was not used and test pieces were cut out from the diameters between 110–125 mm and 175–200 mm. The measured refractive indices showed no positional variation and are 1.534 ± 0.002, 1.540 ± 0.002, and 1.555 ± 0.002 at the 270 GHz, 350 GHz and 670 GHz Bands, respectively, we regard these values as the same at 4K.

Furthermore, the refractive index of HDPE causes a reflective loss of ~ 4 percent which leads not only to decrease in observational efficiency but also to the generation of standing waves and scattered light inside the cryostat. To reduce the surface reflection, lenses have machined antireflective surfaces with concentric circumferential grooves of triangular cross sections. The groove size dimensions are calculated based on the second-order effective medium theory [32]–[34], which resulted in depths of 222 and 171 μm with periods of 434 and 335 μm for the 270 and 350 GHz, of the Phase I bands.

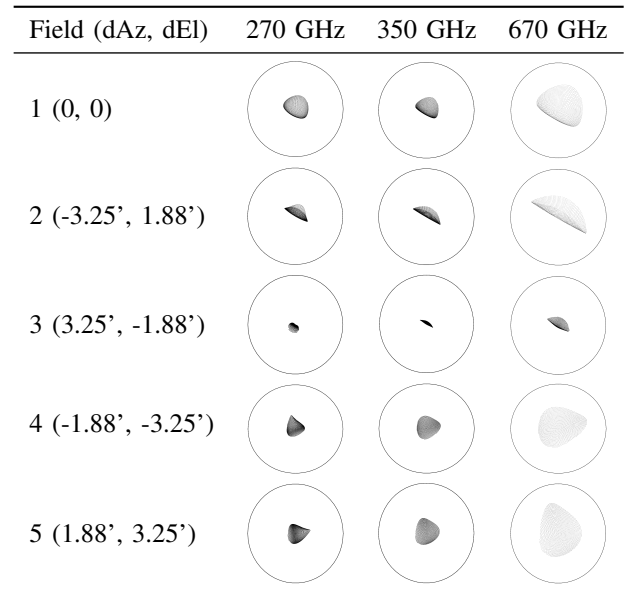| Field (dAz, dEl)	270 GHz	350 GHz	670 GHz
1 (0, 0)			
2 (-3.25', 1.88')			
3 (3.25', -1.88')			
4 (-1.88', -3.25')			
5 (1.88', 3.25')			

Fig. 10. Spot diagram at the focal planes of 270, 350, and 670 GHz bands. Fields 2–5 correspond to the edge of the field of view. The ray spots of all center and edge rays for each band are small enough compared to the Airy discs (black circles), the radii of which are 3377, 3340, and 1768 μm at 270, 350, and 670 GHz, respectively.

We adopt the convex-flat lens without optimizations for the ease of fabrication. The positions of the lenses are determined to realize the focal plane sizes of 55, 70, and 70 mm in diameter for the 270, 350, and 670 GHz Bands. The curvature radii R are calculated to satisfy the condition of telecentric system by the following equation:

$$R = l(n - 1)$$

where l is the length between the cold pupil and the lens surface, and n is the refractive index of HDPE. As a result, we obtain $R = 125.5$, 162.0, and 166.5 mm with the F-numbers of 2.525, 3.233, and 3.233 for the 270, 350, and 670 GHz Bands, respectively.

D. Simulated Performances

To evaluate the imaging quality of this optics design, spot diagrams and Strehl ratios were derived for the field center, 4 grids and 12 grids in radial and circumferential directions, respectively, resulting in 49 positions for each focal plane. Figure 10, which shows the spot diagrams of representative five positions for each focal plane, indicates that rays are confined within the Airy disc. The Strehl ratios of representative nine positions, summarized in Table IV, are used as an indicator of aberration and exceed 0.88, above the commonly used criterion of 0.8, across the FoV. Therefore, diffraction limited optics is obtained.

III. PHYSICAL OPTICS EVALUATION

In order to finalize the camera optics design, evaluation of influences of cold pupil diameter and the horn array position along the optical axis were performed and these dimensions were determined. For this analysis, consideration of diffraction

TABLE IV
STREHL RATIOS AT EACH BAND AND FIELD

Field (dAz, dEl)	270 GHz	350 GHz	670 GHz
1 (0, 0)	0.982	0.987	0.950
2 (-3.25', 1.88')	0.978	0.979	0.923
3 (3.25', -1.88')	0.998	0.995	0.984
4 (-1.88', -3.25')	0.979	0.969	0.892
5 (1.88', 3.25')	0.977	0.966	0.883
6 (-1.62', 0.94')	0.979	0.980	0.926
7 (1.62', -0.94')	0.993	0.996	0.982
8 (-0.94', -1.62')	0.985	0.984	0.940
9 (0.94', 1.62')	0.984	0.984	0.938

TABLE V
PARAMETERS OF BEAM PATTERNS AT EACH BAND AND FIELD

270 GHz	Field1	Field2	Field3	Field4
Gain (dBi)	84.63	84.71	84.07	84.54
Aperture efficiency (%)	36.33	37.00	31.92	35.54
FWHM minor (arcsec)	27.58	27.35	29.95	27.82
FWHM major (arcsec)	28.72	28.30	28.82	28.48
Sidelobe level (dB)	-17.87	-16.50	-17.29	-17.80
Cross pol. level (dB)	-34.62	-34.61	-34.79	-29.02

350 GHz	Field1	Field2	Field3	Field4
Gain (dBi)	86.91	86.89	86.28	86.74
Aperture efficiency (%)	36.50	36.39	31.61	35.15
FWHM minor (arcsec)	21.29	21.25	23.13	21.54
FWHM major (arcsec)	22.14	21.83	22.36	22.02
Sidelobe level (dB)	-17.58	-16.16	-17.45	-17.45
Cross pol. level (dB)	-33.89	-34.26	-34.34	-28.72

670 GHz	Field1	Field2	Field3	Field4
Gain (dBi)	92.23	92.22	91.47	91.69
Aperture efficiency (%)	33.95	33.89	28.50	29.99
FWHM minor (arcsec)	11.14	10.85	12.12	11.37
FWHM major (arcsec)	11.51	11.52	11.68	11.61
Sidelobe level (dB)	-16.89	-15.34	-17.09	-14.77
Cross pol. level (dB)	-35.02	-35.08	-35.15	-28.46

The tables are the cases of 85% diameter of the geometrical pupil and no horn offset.

effect is required. Hence we use the Physical Optics (PO) antenna analysis software GRASP9 [35]. PO is the method to determine the propagation of electromagnetic waves based on Maxwell's equations. The current distribution of a scatterer's surface can be calculated from the beam pattern of the previous scatterer, which is calculated by the current distributions on the previous scatterer. The antenna pattern and spillover of each optical element are also calculated with this method.

A. Model

We make an equivalent model of the designed optics described in Section II, which include the main-reflector, the sub-reflector, the third mirror, the 300 K cryostat window, the 50 K shield window, the 4 K shield window, the cold pupil (dichroic filter), the fourth flat mirror, the dielectric lens, the fifth flat mirror, and the conical horn. All these optical elements except the conical horn are modeled as reflective mirrors with the same aperture size as designed because of their ease of use. The conical horn is modeled using a built-in conical horn feed element, whose parameters are aperture diameter and flare length, and the parameters in Table II are used. A dielectric lens is modeled as a spherical reflector under the assumptions of a thin lens and telecentric optics. Optical components that limit the diameter of the beams, that is, cold pupil, 4 K and 50 K shields, and cryostat windows, are modeled as plane mirrors. This equivalent reflective model has almost the same Strehl ratios (differences are less than 0.04) and spot diagrams over the field of view, therefore, this model is sufficiently plausible for the PO analysis.

Additionally, the blockage of the sub-reflector is treated as a hole on the main-reflector, and the blockage of the sub-reflector supporting structure is neglected. As the surfaces of the optical elements are assumed to be perfect, Ruze losses are neglected. We also do not consider the reflection and absorption losses by the filters and lenses. As an example, in the case of the ASTE telescope, the surface error of $19 \mu m$ decrease the aperture efficiency of 5, 8, and 25 percent at the 270, 350, and 670 GHz Bands, respectively. However, we do not include this loss in the analysis in order to simplify the consideration of diffraction.

We calculate 10 models that have different sizes of cold pupils under the condition that the apertures of the horn arrays coincide with the focal planes, for each 270, 350, and 670 GHz Band. Subsequently, 5 models are calculated by changing the

positions of the horn arrays along the optical axis setting the size of cold pupil as 85 % of the geometrical pupil, for both the 270 and 350 GHz Bands. We analyze four fields of Field 1, 2, 3, and 4, because Fields 4 and 5 are equivalent in this analysis since they are symmetrically-located with respect to the long axis of the third mirror.

B. Results

Each run provides us beam patterns of E-plane, H-plane, and cross polarization (e.g., Figure 11), and some beam parameters, that is, gain, beam size (FWHM), sidelobe level, and cross polarization level are obtained. The aperture efficiency is derived from the gain. An example of those results is summarized in Table V. Spillovers of each optical element are also provided from the each run. We assume that these spillovers are terminated to the appropriate temperature (4 K or 300 K).

C. Discussion

1) Diameter of Cold Pupil: Figure 12 shows the dependencies of the aperture efficiencies and the fractional solid angles of spillovers from 300 K on the size of cold pupil. The aperture efficiencies decrease with the reducing of the size of the cold pupil as the illumination area to the main-reflector becomes smaller. Reducing the cold pupil diameter affects all fields equally and the spillovers from 300 K decreases at first, then stabilizes at ~85 percent of the geometrical pupil diameter. Therefore, we decided to reduce the size of the cold pupil to 85 percent of the diameter of the geometrical design. As summarized in Table V, obtained aperture efficiencies of the beams are $\sim$ 35 %, 35 %, and 32 % with the beam sizes of $\sim$
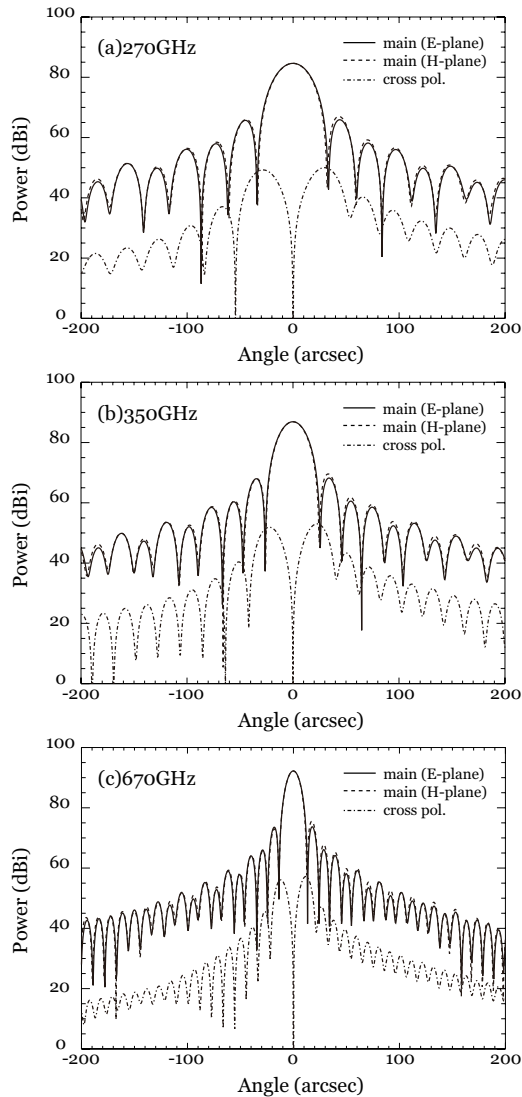
Fig. 11. Beam patterns of the central beam (Field 1) of (a) 270 GHz, (b) 350 GHz, and (c) 670 GHz Bands. These are cases of 85% geometrical pupil diameter and horn offset of $0z_c$.
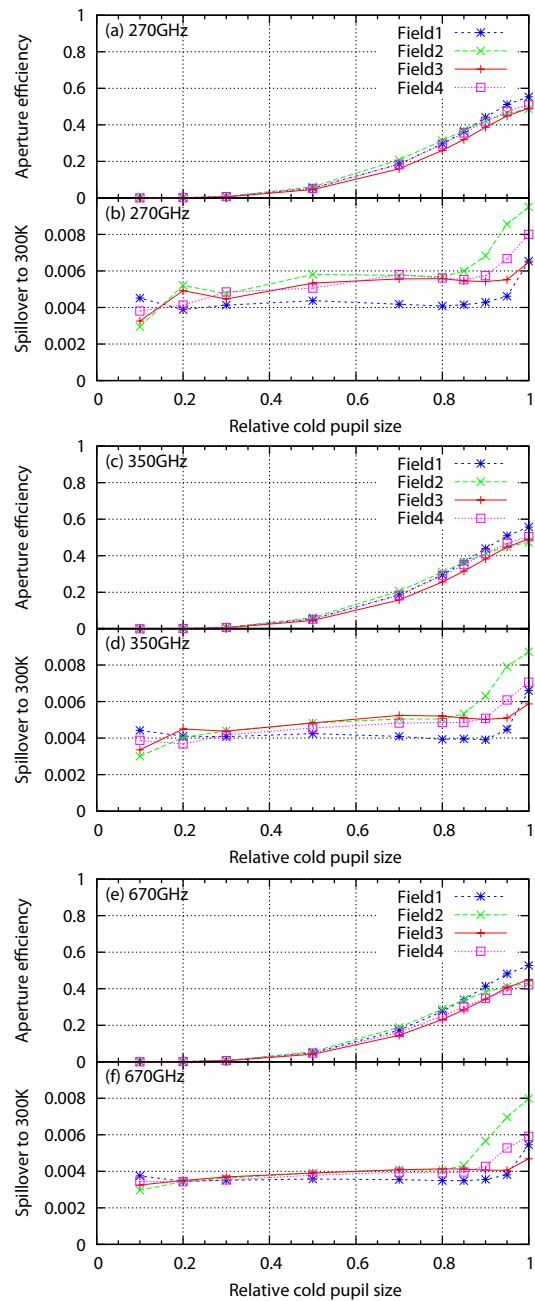

Fig. 12. Aperture efficiency and fractional spillover to 300 K dependencies on the size of the cold pupil in (a, b) 270 GHz, (c, d) 350 GHz, and (e, f) 670 GHz Bands. The size of the cold pupil is normalized by the geometrical pupil diameter.

28, 22, and 12 arcseconds, for 270, 350, and 670 GHz Bands, respectively, and they are all diffraction limited.

2) Horn Array Offset along the Optics Axis: Figure 13 shows the aperture efficiency dependency on the positional offset of the horn array apertures along the optics axis. The improvement in aperture efficiencies by introducing the offset is found to be as small as ~ 1 percent. Therefore, considering the interference with optical components, we decided to place the aperture of the horn array at the focal plane.

IV. SUMMARY

We designed the optics of the multi-color TES bolometer camera for the ASTE telescope. The designed optics fit inside the ASTE cabin and the camera cryostat. The optics for 2-color simultaneous observation and 7.5 arcminute diameter FoV were achieved. We will operate the 270 GHz and 350

GHz Bands for Phase I configuration, and the 350 GHz and 670 GHz Bands for Phase II configuration. The numbers of pixels were optimized to be 169, 271, and 919 pixels for the 270, 350, and 670 GHz Bands, respectively.

We optimized the shape of the third mirror as a modified ellipsoid using ZEMAX software. Dielectric lenses were designed based on the measured values of thermal contraction at 77 K and refractive indices of HDPE at 20 K to be used practically. The estimated thermal contraction from 300 K to 4 K was 2.0 ± 0.1 percent, and this value is consistent with previous studies. The refractive indices of HDPE at ~ 20K
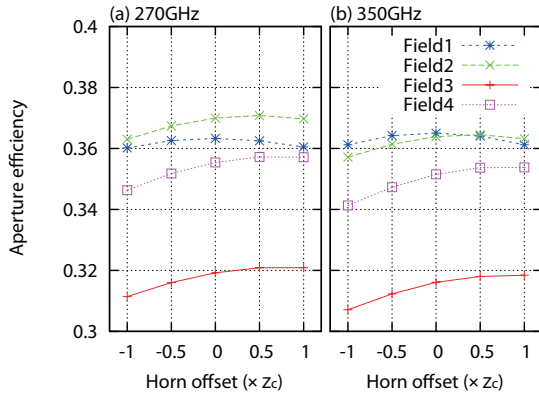
Fig. 13. Aperture efficiency dependencies on the positional offset of the horn array aperture along the optical axis for (a) 270 GHz and (b) 350 GHz bands. The offset of the horn array aperture from the focal plane is normalized by the confocal length z_c of each band, that is 3.945 and 5.105 mm at 270 and 350 GHz, respectively, and its positive value indicates the direction of the horn aperture.

TABLE VI
BAND CONFIGURATION AND OPTICS PERFORMANCES

Phase	I	II
Bands	2	2
Frequency	270/350 GHz	350/670 GHz
Wavelength	1100/850 μm	850/450 μm
Pixels	169/271	271/919
FoV	7.5'	7.5'
Aperture efficiency	35/35%	35/32%
Beam size (FWHM)	28/22"	22/12"

were measured using FTS, and they were 1.534 ± 0.002, 1.540 ± 0.002, and 1.555 ± 0.002 at the 270 GHz, 350 GHz and 670 GHz Bands, respectively. These values were reflected in the design. We checked imaging qualities using spot diagrams and Strehl ratios. Strehl ratios were more than 0.88 across the all focal planes in all frequency bands, and it was confirmed that the designed optics achieved the diffraction limit.

We evaluated the designed optics using the physical optics (PO) method. We made an equivalent model, which consists of the optical elements modeled as reflective elements and a built-in conical horn feed element. We calculated from models that the size of the cold pupil and the position of the horn array along the optical axis change as parameters. The results of the PO calculations provided us with the beam pattern and spillovers of each optical component. As a result, beam parameters such as gain, aperture efficiency, beam size (FWHM), sidelobe level, and cross polarization level were calculated from the beam patterns. PO analyses also provide the spillovers to terminate each optical element. The spillovers from 300 K decrease at first, and then stabilize at ~ 85 % geometrical pupil. Subsequently, we adopted the cold pupil diameter of 85% geometrical design. We also optimized the position of the horn array in terms of aperture efficiency. The offset of the confocal length changed the aperture efficiency by ~ 1 %. We decided to place the aperture of horn array at the focal plane because of the small improvement of aperture efficiency and the interference with optical components.

As a result of optimization, aperture efficiencies of the beams are ~ 35 %, 35 %, and 32 % with the beam sizes (FWHM) of ~ 28, 22, and 12 arcseconds, for the 270, 350, and 670 GHz bands, respectively. The band configuration and optics performances of the new multi-color TES bolometer camera on the ASTE telescope are summarized in Table VI.

ACKNOWLEDGMENT

REFERENCES

[1] K. Coppin, E. L. Chapin, A. M. J. Mortier, S. E. Scott, C. Borys, J. S. Dunlop, M. Halpern, D. H. Hughes, A. Pope, D. Scott, S. Serjeant, J. Wagg, D. M. Alexander, O. Almaini, I. Aretxaga, T. Babbedge, P. N. Best, A. Blain, S. Chapman, D. L. Clements, M. Crawford, L. Dunne, S. A. Eales, A. C. Edge, D. Farrah, E. Gaztañaga, W. K. Gear, G. L. Granato, T. R. Greve, M. Fox, R. J. Ivison, M. J. Jarvis, T. Jenness, C. Lacey, K. Lepage, R. G. Mann, G. Marsden, A. Martinez-Sansigre, S. Oliver, M. J. Page, J. A. Peacock, C. P. Pearson, W. J. Percival, R. S. Priddey, S. Rawlings, M. Rowan-Robinson, R. S. Savage, M. Seigar, K. Sekiguchi, L. Silva, C. Simpson, I. Smail, J. A. Stevens, T. Takagi, M. Vaccari, E. van Kampen, and C. J. Willott, "The SCUBA Half-Degree Extragalactic Survey - II. Submillimetre maps, catalogue and number counts," MNRAS, vol. 372, p. 1621, 2006.

[2] W. S. Holland, E. I. Robson, W. K. Gear, C. R. Cunningham, J. F. Lightfoot, T. Jenness, R. J. Ivison, J. A. Stevens, P. A. R. Ade, M. J. Griffin, W. D. Duncan, J. A. Murphy, and D. A. Naylor, "SCUBA: a common-user submillimetre camera operating on the James Clerk Maxwell Telescope," MNRAS, vol. 303, p. 659, 1999.

[3] E. Kreysa, H. Gemünd, J. Gromke, C. Haslam, L. Reichertz, E. Haller, J. Beeman, V. Hansen, A. Sievers, and R. Zylka, "Bolometer array development at the max-planck-institut für radioastronomie," *Infrared physics & technology*, vol. 40, p. 191, 1999.

[4] D. J. Haig, P. A. R. Ade, J. E. Aguirre, J. J. Bock, S. F. Edgington, M. L. Enoch, J. Glenn, A. Goldin, S. Golwala, K. Heng, G. Laurent, P. R. Maloney, P. D. Mauskopf, P. Rossinot, J. Sayers, P. Stover, and C. Tucker, "Bolocam: status and observations," in *Proc. of SPIE*, C. M. Bradford, P. A. R. Ade, J. E. Aguirre, J. J. Bock, M. Dragovan, L. Duband, L. Earle, J. Glenn, H. Matsuhara, B. J. Naylor, H. T. Nguyen, M. Yun, & J. Zmuidzinas, Ed., vol. 5498, 2004, p. 78.

[5] G. W. Wilson, J. E. Austermann, T. A. Perera, K. S. Scott, P. A. R. Ade, J. J. Bock, J. Glenn, S. R. Golwala, S. Kim, Y. Kang, D. Lydon, P. D. Mauskopf, C. R. Predmore, C. M. Roberts, K. Souccar, and M. S. Yun, "The AzTEC mm-wavelength camera," MNRAS, vol. 386, p. 807, 2008.

[6] K. Kohno, Y. Tamura, B. Hatsukade, K. Nakanishi, D. Iono, T. Takata, G. W. Wilson, M. S. Yun, T. Perera, J. E. Austermann, K. S. Scott, H. Hughes, I. Aretxaga, K. Tanaka, T. Oshima, N. Yamaguchi, H. Matsuo, H. Ezawa, and R. Kawabe, "AzTEC on ASTE Survey of Sub-millimeter Galaxies," in *Panoramic Views of Galaxy Formation and Evolution*, ser. Astronomical Society of the Pacific Conference Series, T. Kodama, T. Yamada, and K. Aoki, Eds., vol. 399, 2008, p. 264.

[7] G. W. Wilson, D. H. Hughes, I. Aretxaga, H. Ezawa, J. E. Austermann, S. Doyle, D. Ferrusca, I. Hernández-Curiel, R. Kawabe, T. Kitayama, K. Kohno, A. Kuboi, H. Matsuo, P. D. Mauskopf, Y. Murakoshi, A. Montaña, P. Natarajan, T. Oshima, N. Ota, T. A. Perera, J. Rand, K. S. Scott, K. Tanaka, M. Tsuboi, C. C. Williams, N. Yamaguchi, and M. S. Yun, "A bright, dust-obscured, millimetre-selected galaxy beyond the Bullet Cluster (1E0657-56)," MNRAS, vol. 390, p. 1061, 2008.

[8] Y. Tamura, K. Kohno, K. Nakanishi, B. Hatsukade, D. Iono, G. W. Wilson, M. S. Yun, T. Takata, Y. Matsuda, T. Tosaki, H. Ezawa, T. A. Perera, K. S. Scott, J. E. Austermann, D. H. Hughes, I. Aretxaga, A. Chung, T. Oshima, N. Yamaguchi, K. Tanaka, and R. Kawabe, "Spatial correlation between submillimetre and Lyman-α galaxies in the SSA22 protocluster," Nature, vol. 459, p. 61, 2009.

[9] K. S. Scott, M. S. Yun, G. W. Wilson, J. E. Austermann, E. Aguilar, I. Aretxaga, H. Ezawa, D. Ferrusca, B. Hatsukade, D. H. Hughes, D. Iono, M. Giavalisco, R. Kawabe, K. Kohno, P. D. Mauskopf, T. Oshima, T. A. Perera, J. Rand, Y. Tamura, T. Tosaki, M. Velazquez, C. C. Williams, and M. Zeballos, "Deep 1.1mm-wavelength imaging of the GOODS-S field by AzTEC/ASTE - I. Source catalogue and number counts," MNRAS, vol. 405, p. 2260, 2010.

[10] Y. Tamura, D. Iono, D. J. Wilner, M. Kajisawa, Y. K. Uchimoto, D. M. Alexander, A. Chung, H. Ezawa, B. Hatsukade, T. Hayashino, D. H. Hughes, T. Ichikawa, S. Ikarashi, R. Kawabe, K. Kohno, B. D. Lehmer, Y. Matsuda, K. Nakanishi, T. Takata, G. W. Wilson, T. Yamada, and M. S. Yun, "Submillimeter Array Identification of the Millimeter-selected Galaxy SSA22-AzTEC1: A Protoquasar in a Protocluster?" ApJ, vol. 724, p. 1270, 2010.

[11] B. Hatsukade, K. Kohno, I. Aretxaga, J. E. Austermann, H. Ezawa, D. H. Hughes, S. Ikarashi, D. Iono, R. Kawabe, S. Khan, H. Matsuo, S. Matsuura, K. Nakanishi, T. Oshima, T. Perera, K. S. Scott, M. Shirahata, T. T. Takeuchi, Y. Tamura, K. Tanaka, T. Tosaki, G. W. Wilson, and M. S. Yun, "AzTEC/ASTE 1.1-mm survey of the AKARI Deep Field South: source catalogue and number counts," MNRAS, vol. 411, p. 102, 2011.

[12] S. Ikarashi, K. Kohno, J. E. Aguirre, I. Aretxaga, V. Arumugam, J. E. Austermann, J. J. Bock, C. M. Bradford, M. Cirasuolo, L. Earle, H. Ezawa, H. Furusawa, J. Furusawa, J. Glenn, B. Hatsukade, D. H. Hughes, D. Iono, R. J. Ivison, S. Johnson, J. Kamenetzky, R. Kawabe, R. Lupu, P. Maloney, H. Matsuhara, P. D. Mauskopf, K. Motohara, E. J. Murphy, K. Nakajima, K. Nakanishi, B. J. Naylor, H. T. Nguyen, T. A. Perera, K. S. Scott, K. Shimasaku, T. Takagi, T. Takata, Y. Tamura, K. Tanaka, T. Tsukagoshi, D. J. Wilner, G. W. Wilson, M. S. Yun, and J. Zmuidzinas, "Detection of an ultrabright submillimetre galaxy in the Subaru/XMM-Newton Deep Field using AzTEC/ASTE," MNRAS, vol. 415, p. 3081, 2011.

[13] I. Aretxaga, G. W. Wilson, E. Aguilar, S. Alberts, K. S. Scott, N. Scoville, M. S. Yun, J. Austermann, T. P. Downes, H. Ezawa, B. Hatsukade, D. H. Hughes, R. Kawabe, K. Kohno, T. Oshima, T. A. Perera, Y. Tamura, and M. Zeballos, "AzTEC millimetre survey of the COSMOS field - III. Source catalogue over 0.72 deg^2 and plausible boosting by large-scale structure," MNRAS, vol. 415, p. 3831, 2011.

[14] K. S. Scott, G. W. Wilson, I. Aretxaga, J. E. Austermann, E. L. Chapin, J. S. Dunlop, H. Ezawa, M. Halpern, B. Hatsukade, D. H. Hughes, R. Kawabe, S. Kim, K. Kohno, J. D. Lowenthal, A. Montaña, K. Nakanishi, T. Oshima, D. Sanders, D. Scott, N. Scoville, Y. Tamura, D. Welch, M. S. Yun, and M. Zeballos, "The source counts of submillimetre galaxies detected at λ= 1.1 mm," MNRAS, vol. 423, p. 575, 2012.

[15] W. Holland, M. MacIntosh, A. Fairley, D. Kelly, D. Montgomery, D. Gostick, E. Atad-Ettedgui, M. Ellis, I. Robson, M. Hollister, A. Woodcraft, P. Ade, I. Walker, K. Irwin, G. Hilton, W. Duncan, C. Reintsema, A. Walton, W. Parkes, C. Dunare, M. Fich, J. Kycia, M. Halpern, D. Scott, A. Gibb, J. Molnar, E. Chapin, D. Bintley, S. Craig, T. Chylek, T. Jenness, F. Economou, and G. Davis, "SCUBA-2: a 10,000-pixel submillimeter camera for the James Clerk Maxwell Telescope," in Proc. of SPIE, vol. 6275, 2006.

[16] G. Siringo, E. Kreysa, A. Kovács, F. Schuller, A. Weiß, W. Esch, H.-P. Gemünd, N. Jethava, G. Lundershausen, A. Colin, R. Güsten, K. M. Menten, A. Beelen, F. Bertoldi, J. W. Beeman, and E. E. Haller, "The Large APEX BOlometer CAmera LABOCA," A&A, vol. 497, p. 945, 2009.

[17] M. W. Werner, T. L. Roellig, F. J. Low, G. H. Rieke, M. Rieke, W. F. Hoffmann, E. Young, J. R. Houck, B. Brandl, G. G. Fazio, J. L. Hora, R. D. Gehrz, G. Helou, B. T. Soifer, J. Stauffer, J. Keene, P. Eisenhardt, D. Gallagher, T. N. Gautier, W. Irace, C. R. Lawrence, L. Simmons, J. E. Van Cleve, M. Jura, E. L. Wright, and D. P. Cruikshank, "The Spitzer Space Telescope Mission," ApJS, vol. 154, p. 1, 2004.

[18] G. L. Pilbratt, J. R. Riedinger, T. Passvogel, G. Crone, D. Doyle, U. Gageur, A. M. Heras, C. Jewell, L. Metcalfe, S. Ott, and M. Schmidt, "Herschel Space Observatory. An ESA facility for far-infrared and submillimetre astronomy," A&A, vol. 518, p. L1, 2010.

[19] H. Ezawa, R. Kawabe, K. Kohno, and S. Yamamoto, "The Atacama Submillimeter Telescope Experiment (ASTE)," in Proc. of SPIE, vol. 5489, 2004, p. 763.

[20] H. Ezawa, K. Kohno, R. Kawabe, S. Yamamoto, H. Inoue, H. Iwashita, H. Matsuo, T. Okuda, T. Oshima, T. Sakai et al., "New achievements of ASTE: the Atacama Submillimeter Telescope Experiment," in Proc. of SPIE, vol. 7012, 2008.

[21] S. Matsushita, H. Matsuo, J. R. Pardo, and S. J. E. Radford, "FTS Measurements of Submillimeter-Wave Atmospheric Opacity at Pampa la Bola II : Supra-Terahertz Windows and Model Fitting," PASJ, vol. 51, p. 603, 1999.

[22] A. Kovács, "CRUSH: fast and scalable data reduction for imaging arrays," in Proc. of SPIE, vol. 7020, 2008.

[23] E. Shirokoff, B. Benson, L. Bleem, C. Chang, H. Cho, A. Crites, M. Dobbs, W. Holzapfel, T. Lanting, A. Lee et al., "The south pole telescope sz-receiver detectors," IEEE Trans. Appl. Supercond., vol. 19, p. 517, 2009.

[24] B. Westbrook, A. Lee, X. Meng, A. Suzuki, K. Arnold, E. Shirokoff, E. George, F. Aubin, M. Dobbs, K. MacDermid, S. Hanany, K. Raach, A. Aboobaker, J. Hubmayr, T. Oshima, M. Kawamura, and K. Kohno, "Design Evolution of the Spiderweb TES Bolometer for Cosmology Applications," Journal of Low Temperature Physics, vol. 167, p. 885, 2012.

[25] D. Schwan, P. A. R. Ade, K. Basu, A. N. Bender, F. Bertoldi, H. Cho, G. Chon, J. Clarke, M. Dobbs, D. Ferrusca, R. Gusten, N. W. Halverson, W. L. Holzapfel, C. Horellou, D. Johansson, B. R. Johnson, J. Kennedy, Z. Kermish, R. Kneissl, T. Lanting, A. T. Lee, M. Lueker, J. Mehl, K. M. Menten, D. Muders, F. Pacaud, T. Plagge, C. L. Reichardt, P. L. Richards, R. Schaaf, P. Schilke, M. W. Sommer, H. Spieler, C. Tucker, A. Weiss, B. Westbrook, and O. Zahn, "Invited article: Millimeter-wave bolometer array receiver for the atacama pathfinder experiment sunyaev-zel'dovich (apex-sz) instrument," Review of Scientific Instruments, vol. 82, p. 091301, 2011.

[26] P. Ade, G. Pisano, C. Tucker, and S. Weaver, "A review of metal mesh filters," in Proc. of SPIE, vol. 6275, 2006.

[27] T. Klaassen, M. Diez, J. Blok, C. Smorenburg, K. Wildeman, and G. Jakob, "Optical characterization of absorbing coatings for sub-millimeter radiation," in Proceedings of the 12 th International Symposium on Space THz Technology, 2001, p. 400. [Online]. Available: http://www.nrao.edu/meetings/isstt/papers/2001/2001400409.pdf

[28] ZEMAX Development Corp., 3001 112th Avenue NE, Suite 202, Bellevue, WA 98004.

[29] J. Birch, J. Dromey, and J. Lesurf, "The optical constants of some common low loss polymers between 4 and 40 cm," Infrared Physics, vol. 21, p. 225, 1981.

[30] R. Corruccini and J. Gniewek, "Thermal expansion of technical solids at low temperatures," NATIONAL BUREAU OF STANDARDS MONOGRAPH 29, 1961.

[31] G. Schwarz, "Thermal expansion of polymers from 4.2 K to room temperature," Cryogenics(Guildford), vol. 28, p. 248, 1988.

[32] A. Wagner-Gentner, U. Graf, D. Rabanus, and K. Jacobs, "Low loss THz window," Infrared Physics and Technology, vol. 48, p. 249, 2006.

[33] D. Raguin and G. Morris, "Analysis of antireflection-structured surfaces with continuous one-dimensional surface profiles," Appl. Opt., vol. 32, p. 2582, 1993.

[34] ——, "Antireflection structured surfaces for the infrared spectral region," Appl. Opt., vol. 32, p. 1154, 1993.

[35] TICRA, Læderstræde 34, DK-1201 Copenhagen K, Denmark.

Tatsuya Takekoshi was born in Hokkaido, Japan in 1985. He received the degrees of B.S. in Physics and M.S in Cosmoscience from Hokkaido University, Sapporo, Japan in 2008 and 2010, respectively. His current research interests are development of the multi-color TES bolometer camera for the ASTE telescope, and an observational study of starformation process in the low metallicity environment using millimeter and submillimeter instruments.